JOURNAL OF GEOPHYSICAL RESEARCH, VOL. 111, C11S22, doi:10.1029/2005JC003246, 2006

Contrasts in sea ice deformation and production in the Arctic seasonal and perennial ice zones

R. Kwok[1]

Received 24 August 2005; revised 16 December 2005; accepted 3 May 2006; published 16 August 2006.

[1] Four years (1997–2000) of RADARSAT Geophysical Processor System (RGPS) data are used to contrast the sea ice deformation and production regionally, and in the seasonal (SIZ) and perennial (PIZ) ice zones. Ice production is of seasonal ice in openings during the winter. Three-day estimates of these quantities are provided within Lagrangian elements initially 10 km on a side. A distinct seasonal cycle is seen in both zones with these estimates highest in the late fall and with seasonal minimums in the midwinter. Regional divergence over the winter could be up to 30%. Spatially, the highest deformation is seen in the SIZ north of coastal Alaska. Both ice deformation and production are higher in the SIZ: deformation-related ice production in the SIZ ($\sim$0.5 m) is 1.5–2.3 times that of the PIZ ($\sim$0.3 m): this is connected to ice strength and thickness. Atmospheric forcing and boundary layer structure contribute to only the seasonal and interannual variability. Seasonal ice growth in ice fractures accounts for $\sim$25–40% of the total ice production of the Arctic Ocean. Uncertainties in these estimates are discussed. By itself, this deformation-ice production relationship could be considered a negative feedback when thickness is perturbed. However, the overall effect on ice production in the face of increasing seasonal and thinner/weaker ice coverage could be modified by local destabilization of the water column promoting overturning of warmer water due to increased brine rejection; and the upwelling of the pynocline associated with increased occurrence of large shear motion in sea ice. Divergence is shown to be negligibly correlated to cyclonic motion in summer and winter in both ice zones.

Citation: Kwok, R. (2006), Contrasts in sea ice deformation and production in the Arctic seasonal and perennial ice zones, *J. Geophys. Res.*, *111*, C11S22, doi:10.1029/2005JC003246.

1. Introduction

[2] The small-scale dynamic response of the winter sea ice cover to gradients in large-scale surface wind stress is localized along quasi-linear fractures where openings and closings are found. These fractures, with widths of kilometers and lengths up to hundreds of kilometers, are resolved in high-resolution imagery and derived motion fields from synthetic aperture radar (SAR) data. Newly opened leads are a source of new ice growth, brine rejection to the ocean, and rapid heat transfer from the ocean to the atmosphere. These areas dominate the local heat flux into the atmosphere and brine flux into the mixed layer. Closings of the ice cover cause ice to raft and to pile up into pressure ridges and forced down into keels increasing the ice-atmosphere and ice-ocean drag. Compared to thermodynamics, these dynamic processes alter the thickness distribution of the Arctic Ocean ice cover at much smaller length scales.

[3] An accurate ice dynamics model for climate studies must reflect the appropriate proportions of these processes (opening/closing) as well as their beginning and end states. Differentiation of the openings and closings is important because of their distinct expressions in the ice thickness distribution. Estimates of divergence and convergence from buoy drift provide only large-scale sums of these quantities. Only with sea ice kinematics derived from high resolution SAR imagery have we been able to approach the spatial length scale required to separate these processes. In the late 1980s and for most of the 1990s, the availability of small volumes of ice motion data from the European SAR satellites (ERS-1, 2) have allowed a more detailed look at the deformation of the ice cover: *Fily and Rothrock* [1990] examined digital methods to determine the linear openings and closings in the ice cover; *Stern et al.* [1995] studied the parameterization of open water production based on area-averaged deformation; *Cunningham et al.* [1994] measured the orientation of newly-opened leads in a small number of SAR images; and, *Overland et al.* [1998] used SAR ice motion to examine the granular-plastic properties of sea ice and reviewed the history of leads and their interpretations.

[4] Launched in November 1996, RADARSAT with its wide-swath mode provides routine near basin-scale cover-

[1]Jet Propulsion Laboratory, California Institute of Technology, Pasadena, California, USA.

0148-0227/06/2005JC003246$09.00

age of the Arctic Ocean at high resolution (~100 m). The fine-scale sea ice kinematics produced by the RADARSAT Geophysical Processor System (RGPS) resolve fracture patterns, and offer a level of spatial and temporal detail that allows for a closer examination of small-scale deformation at a near basin-scale context. Dense 3-day ice trajectories (~10 km sample spacing) over four years are now available. These products have been used to drive a granular model of sea ice [*Hopkins et al.*, 1999] and a single-column ice thickness model [*Curry et al.*, 2001]. The strain rates have also been used in a study to relate Arctic pack ice stress and deformation [*Richter-Menge et al.*, 2002] and in a study of rafting and redistribution of ice thickness [*Babko et al.*, 2002]. The ice motion data have been used in a data fusion study to derive the best estimate of ice deformation near SHEBA [*Lindsay*, 2002]. *Coon et al.* [1998] and *Hibler and Schulson* [2000] have used the deformation patterns to understand the modeling implications of an anisotropic ice cover.

[5] Estimates of seasonal ice production in fractures, from a record of openings and closings in Lagrangian elements, are also derived from the small-scale RGPS sea ice kinematics. The present note examines the large-scale relationship between deformation and ice production over the Arctic Ocean ice cover as depicted by the RGPS data set. A large-scale multiseasonal estimate of this sort, constrained by observed sea ice deformation, has never been attempted. With these estimates, we address the following questions: What is the regional and seasonal dependence and variability of ice deformation and ice production? What is the difference between ice deformation and production in the seasonal and perennial ice zones? What is the contribution of ice production in fractures to the mass budget and ice production in the Arctic Ocean? What are the potential implications of a thinning ice cover?

[6] This paper is organized as follows. The data sets used in this paper are described next. Section 3 provides an overview of the ice conditions of the four winters covered by the RGPS data set. The seasonal, regional, and ice condition dependence of deformation activity and variability are explored in section 4. The relationship of ice production to the spatial and temporal character of deformation is discussed in section 5. The contribution of ice production to the Arctic Ocean mass budget is estimated here. Conclusions are given in the last section.

2. Data Description

2.1. RGPS Data Set

[7] For more than seven years, beginning in November of 1996, RADARSAT has provided routine high-resolution SAR mappings of the western Arctic Ocean at ~3-day intervals. The sampling period of ~3 days is determined by available data allocation even though a shorter sampling interval would be more optimal for small-scale kinematics. Acquired radar data are downlinked and processed at the Alaska Satellite Facility (ASF) in Fairbanks, Alaska. The resultant sea ice imagery is analyzed by procedures implemented in the RADARSAT Geophysical Processor System (RGPS). Primary estimates from the RGPS are arrays of sea ice trajectories starting from an initial uniform-spaced grid of ~10 km. *Lindsay and Stern* [2003] report that the median magnitude of displacement differences between buoy drift and RGPS motion estimates is 323 m; this uncertainty in RGPS displacements is comparable to those from drifting buoys. Secondary procedures in the RGPS derive estimates of deformation, histogram of thin ice thickness, and multiyear ice coverage from the record of time-varying backscatter and cell areas computed on the deforming Lagrangian grid. The histogram is of the ice thickness distribution of seasonal ice produced in openings during the winter. Line segments connecting the grid points define cells within which these quantities are computed. Details of the analysis procedures can be found in *Kwok et al.* [1995] and *Kwok and Cunningham* [2002].

[8] The RGPS data set used here consists of products from four winters (1996–1997, 1997–1998, 1998–1999, 1999–2000) and three summers (1997, 1998, 1999). Winters span the period between October and May, and summers between May and August. Gaps in the ice motion data sets are due to the lack of backscatter contrast for tracking ice features in the SAR imagery.

[9] Of the RGPS products, three are used here: ice motion, deformation, and ice thickness. The ice deformation product contains the geographic location, the area, and the velocity gradients of each cell at every time step. Similarly, a record of the derived thickness histograms and multiyear ice coverage estimates at these cells are stored in the ice thickness histogram product.

2.2. Other Data Sets

[10] Six-hourly sea-level pressure (SLP) fields are from the National Centers for Environmental Prediction (NCEP) – National Center for Atmospheric Research (NCAR) reanalysis products [*Kalnay et al.*, 1996]. The monthly Arctic Oscillation (AO) indices are those of the Climate Prediction Center and are constructed using daily 1000 mb height anomalies poleward of 20°N.

3. First-Year and Multiyear Ice Coverage

[11] Ice conditions during the winter are best-described using ice thickness. In the absence of these observations, we use as proxy indicators the two primary ice types: first-year and multiyear ice. In the RGPS, a backscatter-based procedure [*Kwok et al.*, 1992] classifies the SAR image pixels within each Lagrangian cell as members of one of these two types. Broad assessments of the quality of these estimates can be found in *Kwok and Cunningham* [2002] and *Kwok* [2002]. These estimates have been shown to satisfy, to within several percent, the seasonal constraint that no MY ice is created during the winter.

[12] The multiyear (MY) ice coverage in January of 1997, 1998, 1999, and 2000 are shown in Figure 1. Of the four winters, January 97 (Figure 1a) has the most extensive coverage. The perennial ice edge is the farthest south relative to the other years. The remaining winters saw significant decreases in the MY coverage in the region north and west of Wrangel Island compared to the winter of 1997. This large expanse of seasonal ice can be expected to be thinner and mechanically weaker compared to that ice

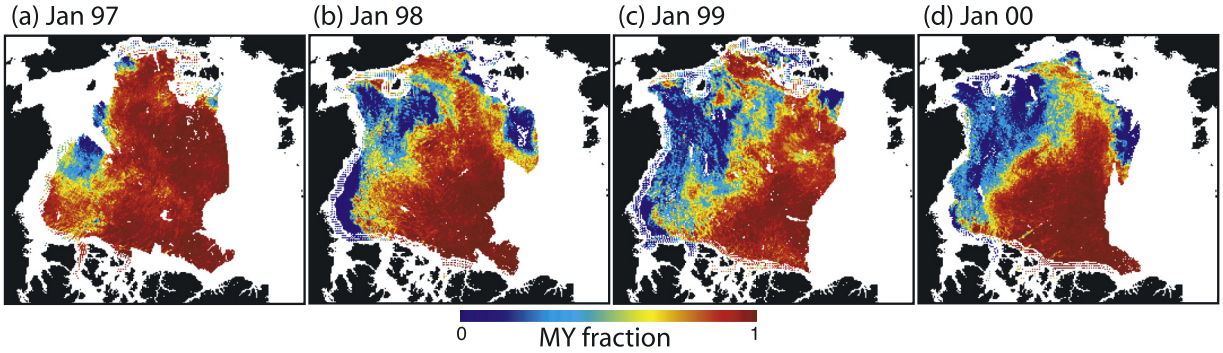

Figure 1. January multiyear ice coverage from RGPS data set. (a) 1997. (b) 1998. (c) 1999. (d) 2000. Note the increasing expanse of seasonal ice in the Beaufort and Chukchi Seas.

within the perennial ice zone (PIZ). Here, we define the PIZ as those regions with >80% MY ice coverage.

4. Sea Ice Deformation

[13] Here, we examine the deformation characteristics of the Arctic Ocean sea ice cover using the four-year RGPS data set. The regional character of deformation and its dependence on whether it is located in the perennial or seasonal ice zone are discussed. The relationships between divergence and vorticity in the two zones are examined.

[14] The divergence, vorticity, and shear (strain rates) of each cell are computed via:

$$\nabla \cdot u = u_x + v_y, \qquad \zeta = v_x - u_y,$$
$$e = \left[\left(u_x - v_y\right)^2 + \left(u_y + v_x\right)^2 \right]^{\frac{1}{2}} \tag{1}$$

u_x, u_y, v_x, v_y are the spatial gradients in ice motion computed using a line integral around the boundary of each cell (~10 km on a side). The line segments connecting the four vertices of a cell define the boundaries. $\nabla \cdot u$ is a measure of the rate of area change, ζ is the principal measure of rotation rate, and e is the scalar magnitude of shear.

4.1. Regional Deformation

[15] Deformation characteristics are examined in five subregions (Figure 2). Henceforth, we designate subregion i as S_i. The sea ice cover of the Beaufort and Chukchi Seas, in S_1 and S_2, are predominantly seasonal and thus thinner. S_3 contains a mixture of ice types with seasonal ice in the south. S_4 and S_5, the central Arctic and Canada Basin, are inside the PIZ and generally have higher fractions of multiyear ice. All regions, except for S_4, are subject to direct coastal influences from the perspective of ice mechanics and thermodynamics. In the fall, the southern boundaries of S_1 and S_2 are exposed to the open ocean.

[16] Figures 2b, 2e, 2h, and 2k show the location and deformation of the boundaries of the five subregions at the end of April; their initial location and coverage in November are shown in Figures 2a, 2d, 2g, and 2j. Displacements of region boundaries are from RGPS ice motion. Net divergence is the sum of cell divergences within each region over the winter. Several motion trajectories (each consisting of ~20 observations) within each region are selected to illustrate the variability of the ice motion and their net displacements over the 6-month period. At the large scale, the mean advection of the subregions and their defining boundaries are expressions of the large-scale circulation patterns forced by the SLP distributions shown in Figures 2c, 2f, 2i, and 2l. At the small scale, the response of the ice cover to large-scale gradients is concentrated in narrow zones of fractures and these give the boundaries the smaller scale structures not resolved in Figure 2. Table 1 (plotted in Figure 3) contrasts the net regional divergence and change in deformed cell coverage of the four winters. For reference, the net deformation at the cell level between November and April is depicted in Figure 4. The net deformation at each cell is computed by first summing the velocity gradients over the period and then calculating the divergence, vorticity, and shear in equation (1). Figure 4 provides a more detailed picture than the regional summaries (Figure 2) discussed below.

[17] On November 7, 1996 the RGPS cells cover an area of 2.52×10^6 km^2 of the Arctic Ocean. At the end of the period (November 7, 1996–April 30, 1997), the same cells cover an area of 2.59×10^6 km^2, with a net divergence of ~2.1% over the 6-month period. During this period, both S_1 and S_2 advected west towards the Siberian coast as part of the Beaufort Gyre. The southern boundary of S_3 next to the New Siberian Islands has pulled away from the coast and moved poleward. S_4 remains relatively undeformed but rotated clockwise with the Beaufort Gyre. Its western boundary moved poleward as part of the Transpolar Drift Stream. Convergence of the ice cover on the Canadian archipelago produced noticeable deformation in S_5. Part of S_5 has advected eastward and some of the cells from this region have actually exited the Arctic Ocean through the Fram Strait.

[18] The initial area of the domain during the second winter (97–98) is $\sim 2.51 \times 10^6$ km^2. The deformation and motion of the ice cover, as illustrated in Figure 2, are quite different from that of previous year. As a result of a well-developed Beaufort Gyre centered over the western Canada Basin, a strong westward ice motion off the Alaska coast carried S_1 far towards Wrangel Island. This can be seen in the large net displacements of the sample RGPS trajectories. The divergence (~25%) of S_1 is more than 3 times that of 96/97 (Figure 3). Of the four winters, this is the only year with a negative Arctic Oscillation (AO) index (−0.7). The AO is the dominant pattern of non-seasonal sea-level pressure (SLP) variations north of 20°N, and it is characterized by SLP anomalies of one sign in the Arctic and

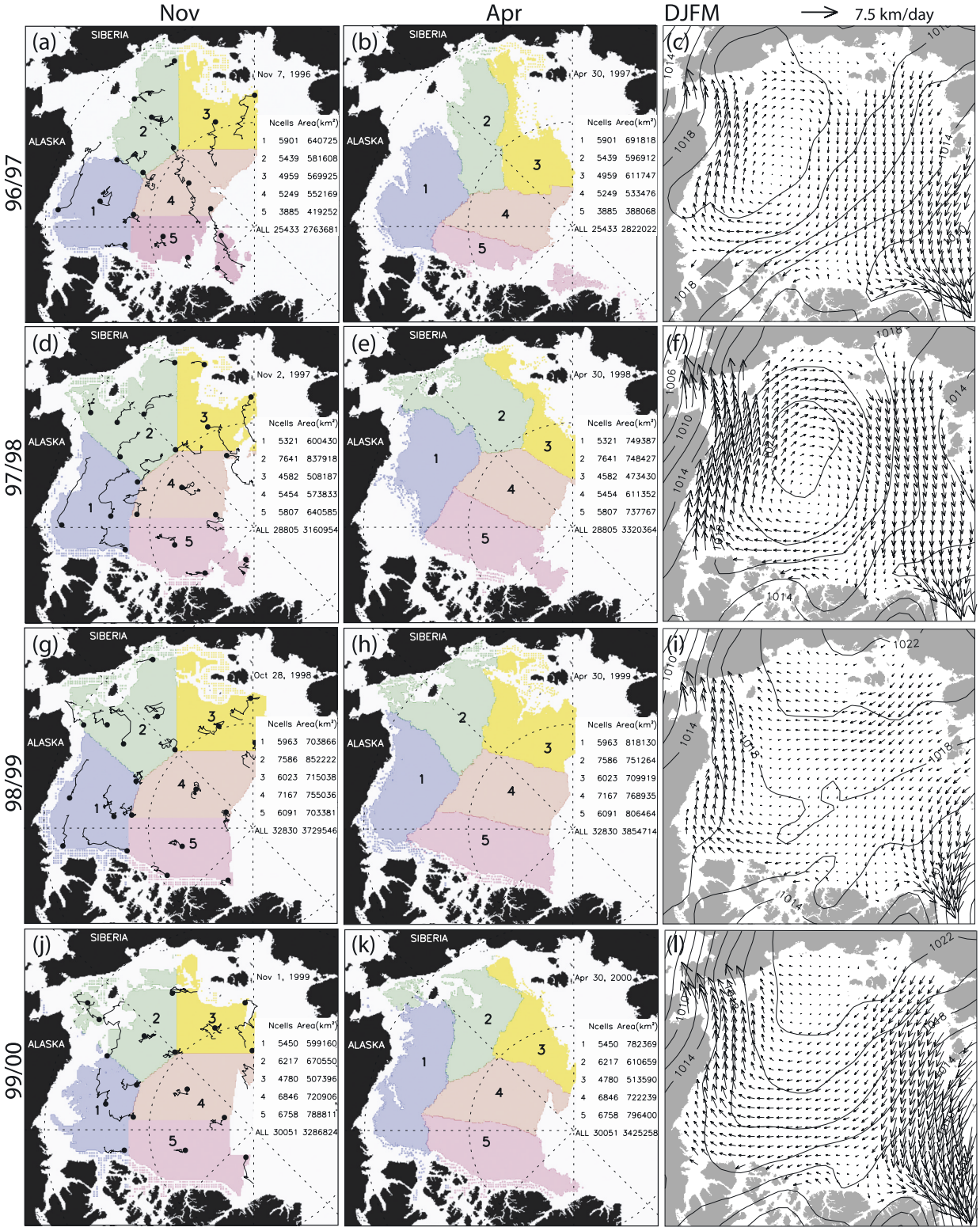

Figure 2. Net deformation of the ice cover between November and April and the mean DJFM ice motion. (a–c) 96/97. (d–f) 97/98. (g–i) 98/99. (j–l) 99–00. Solid circles mark the initial location of select RGPS ice motion trajectories in Figures 2a, 2d, 2g, and 2j. Mean sea-level pressure distributions during the period are contoured. (Isobar intervals: 2 hPa.)

Table 1. Regional Divergence (November Through April)

Percent	S_1	S_2	S_3	S_4	S_5	Net
1996/1997	8.0	2.6	7.3	−3.4	−7.4	2.1
1997/1998	24.8	−10.7	−6.8	6.5	15.2	5.0
1998/1999	16.2	−11.9	−0.7	1.8	14.7	3.4
1999/2000	30.6	−8.9	1.2	0.2	1.0	4.2

anomalies of opposite sign centered about 37–45°N [*Thompson and Wallace*, 1998]. The coherent clockwise rotation of S_3, S_4, and S_5, due to the strength and location of the Beaufort high-pressure cell is evident and is characteristic of seasons with a negative Arctic Oscillation (AO) index [*Kwok*, 2000]. The coverage of negative vorticity cells (blue in Figure 4b – rotation of ∼−30°) shows the dominant anticyclonic rotation experienced by a large part of the ice cover not seen in the other years. Remarkably, net divergences of 7% and 15% can be seen in S_4 and S_5 where convergent ice motion is typically expected. The opposite is true for S_2 and S_3 where net convergences of −11% and −7% are observed at the end of the six months. S_2 is pushed against the Siberian Coast. With the significant divergence in S_1, the entire domain covers $\sim 3.32 \times 10^6$ km^2 at the end of April, 1998 giving the largest net divergence (5%) of the four years. The net divergences of all subregions, except for S_1, have opposite polarities than the first winter. A more detailed analysis of the sea ice kinematics in the vicinity of the SHEBA (Surface Heat Budget of the Arctic Ocean) ice station during this winter can be found in *Stern and Moritz* [2002].

[19] Compared to other years, the winter of 98/99 saw the flattest DJFM SLP field over the central Arctic Ocean. As a result, S_3 and S_4 saw negligible net divergence. It is evident from the RGPS motion trajectories that the net advection of these two regions is small. Overall, S_1 and S_2 have advected west towards the Siberian coast with a large divergence (16%) in the former balanced by a convergence (−12%) in the latter. Similar to the previous year, this is due to significant convergence on the Siberian Coast. The divergence in S_5 is associated with the net southward extension of the region.

[20] Even though a dominant east-west motion of the ice cover can be seen off the Alaska Coast in winter of 99/00, the Beaufort Gyre is not as well-developed as in 97/98. In fact, the AO index of this season, at 0.7, is the highest of the four years. The circulation and SLP distribution seem characteristic of a positive AO winter: there are no closed isobars over the Arctic Ocean and a weak Transpolar Drift Stream [*Kwok*, 2000]. Again, S_1 and S_2 are advected west towards the Siberian coast with a large divergence (31%) in the former balanced by significant convergence (−9%) in the latter. The net divergence of S_3 is highest of the four years. S_3, S_4 and S_5 experienced negligible net divergence. Net regional divergence of the five subregions is ∼4%.

4.2. Deformation in the Perennial and Seasonal Ice Zones

[21] The mean monthly shear deformation, for the four winters, at the RGPS cells is depicted in Figure 5. It can be seen that nearly all deformation are localized along quasi-linear features while large regions of the ice cover remain rigid (yellow), with little or no deformation. Because of the extensive deformation in the regions north of the Alaska coast and west of the Canadian Archipelago, individual linear features are sometimes obscured because of the density of deformed cells. The organization, orientation, and persistence of these linear features are discussed briefly in *Kwok* [2001]. The 80% MY concentration isopleths (black contour) on Figure 5 show that the predominance of deformation activity is outside the PIZ. To add to this view, Figure 6 shows the fractional number of time steps a cell has deformed between Nov–Dec, Jan–Feb, Mar–Apr. Over a time step (∼3 days), we consider a cell to be deformed if the magnitude of divergence is greater than 0.02/day or the magnitude of shear is greater than 0.03/day. These thresholds serve to eliminate noisy samples that are due to uncertainties in the motion estimates. The distinction in the deformation experienced by the two zones is clearly illustrated, especially in November and December.

[22] To quantify the deformation of the ice cover in the perennial (MY fraction >0.8) and seasonal ice zones, we first plot the fractional coverage of deformed cells in the two zones (Figure 7a). This provides a measure of the relative abundance of deformed cells. For all winters, it can be seen

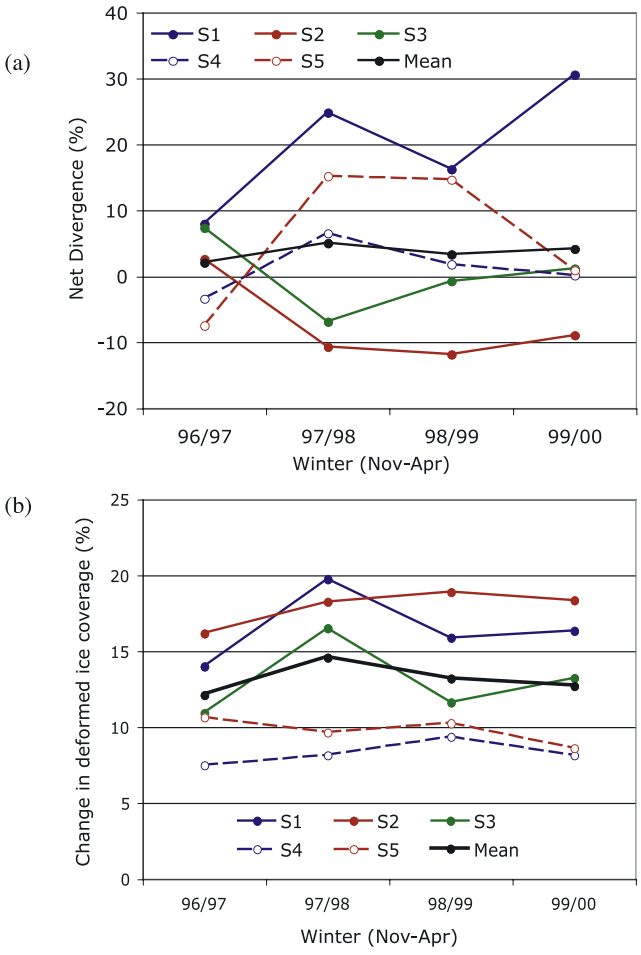

Figure 3. (a) Net divergence and (b) change in deformed ice coverage in S_1, S_2, S_3, S_4, and S_5 at the end of April.

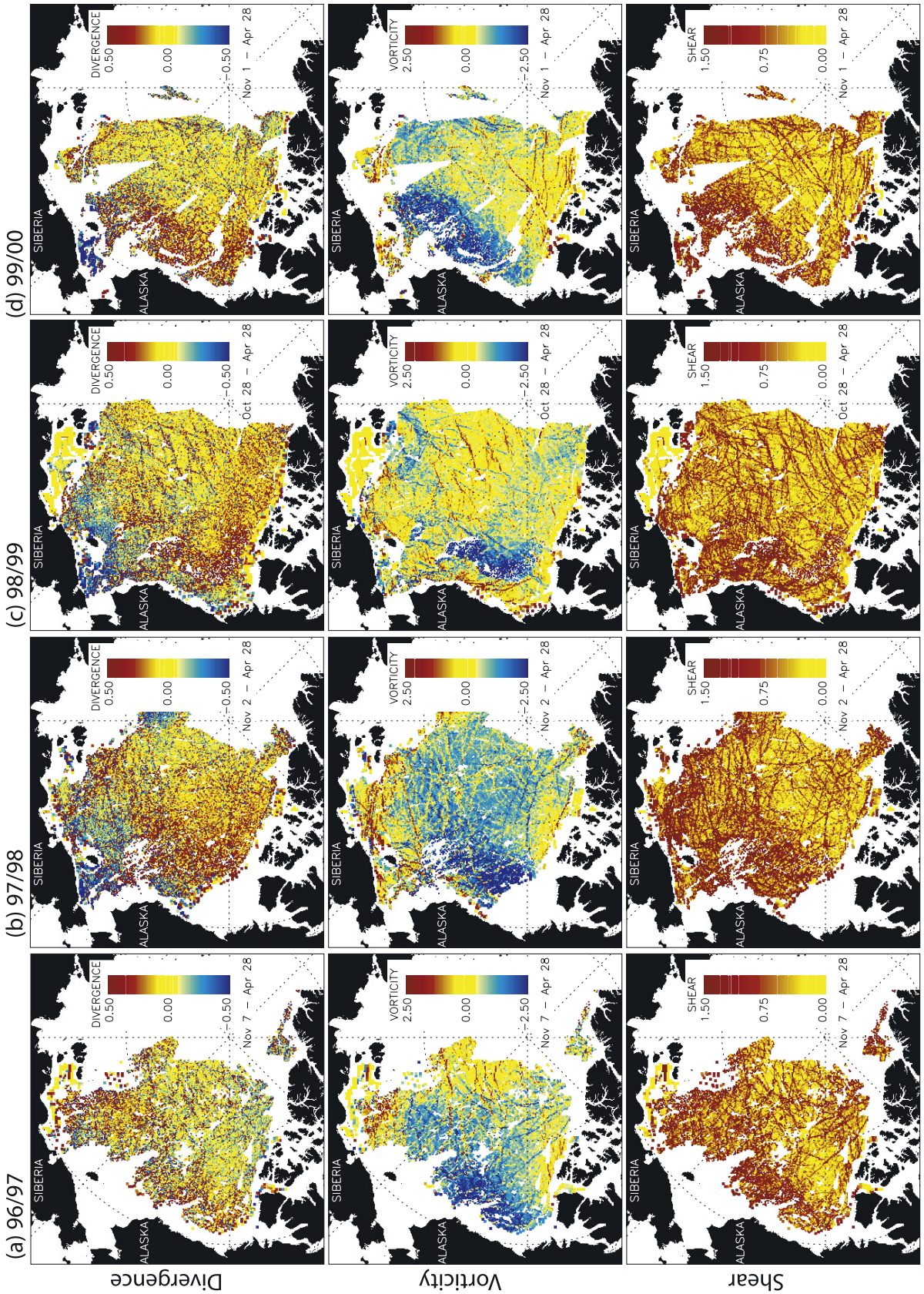

Figure 4. Net divergence, shear, and vorticity of the sea ice cover between November and April. (a) 96/97. (b) 97/98. (c) 98/99. (d) 99–00. The net deformation at each cell, at the end of April, is computed by first summing the velocity gradients over the period and then calculating the net divergence, vorticity, and shear.

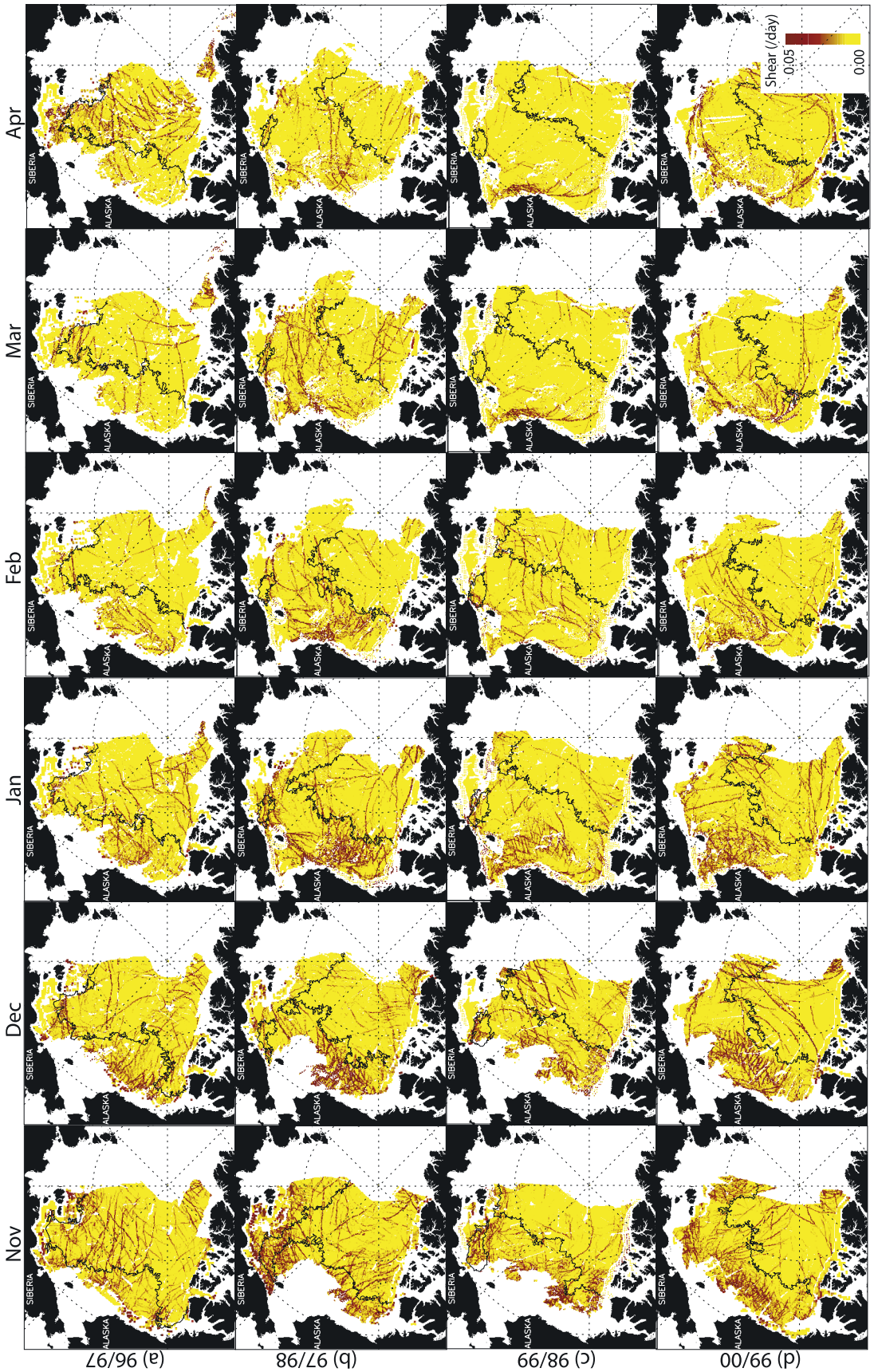

Figure 5. Monthly mean shear at RGPS Lagrangian cells. (a) Nov 96–Apr 97. (b) Nov 97–Apr 98. (c) Nov 98–Apr 99. (d) Nov 99–Apr 00. Black contour is the 80% MY concentration isopleth from Figure 1.

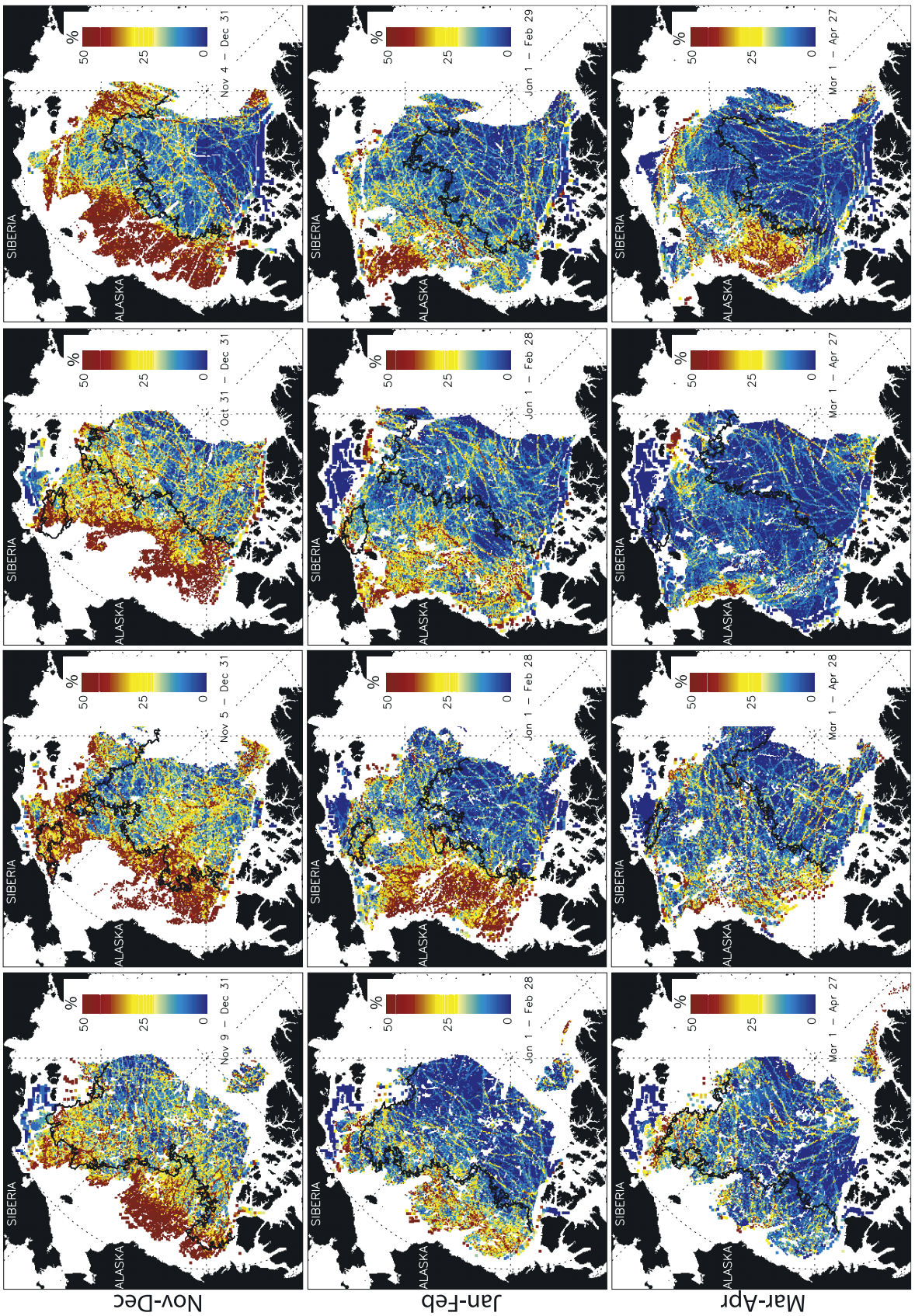

Figure 6. Fractional number of time-steps (in percent) a cell is active between Nov–Dec, Jan–Feb, Mar–Apr. (a) 96/97. (b) 97/98. (c) 98/99. (d) 99/00. A cell is considered active if the magnitude of divergence is greater than 0.02/day or the magnitude of shear is greater than 0.03/day. Black contour is the 80% MY concentration isopleth from Figure 1.

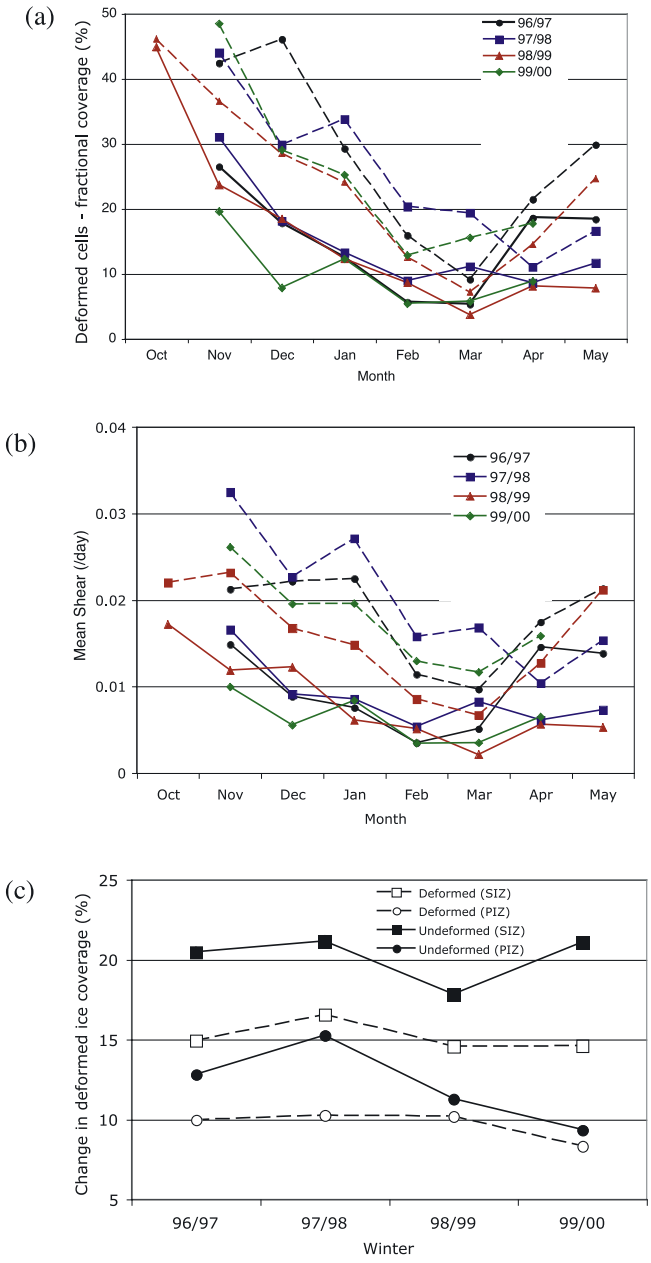

Figure 7. Mean monthly deformation in the perennial and seasonal ice zones. (a) Fractional coverage of deformed cells. (b) Mean monthly shear. (c) Change in deformed ice coverage between November and April. Quantities in the seasonal and perennial ice zones are plotted as dashed and solid lines, respectively.

that there is a higher fraction of deformed cells in the SIZ. In January, the fractional coverage of deformed cells in the SIZ is ~30% compared to the 15% coverage in the perennial ice zone. This ratio is especially pronounced during the late fall and early winter. The fractional coverage of deformed cells also exhibits a definite seasonality with the coverage highest in October and November and lowest in February and March; it then starts to increase with the onset of spring in April and May.

[23] Next, we examine the relative magnitude of the shear in the two zones (Figure 7b). Higher mean deformation (shear) is seen in the seasonal ice zone for all years. The monthly mean also exhibit a seasonal trend with higher deformation in the late fall and spring compared to mid-winter. In November, deformed cells occupy >40% of the area of the SIZ while they occupy only ~25% in the PIZ. In March, the fractional coverage reduces to less than 20% in the SIZ and 10% in the PIZ. Clearly this seasonal trend in the abundance of deformed cells and the magnitude of shear deformation is partly due to increasing thickness and therefore mechanical strength through the winter and partly due to the seasonal structure of the atmospheric boundary layer (reduced momentum transfer due to the stability effects in winter). In one study, *Yu et al.* [2001] find that ice strengths are low in early winter in the SIZ and nearly doubled in the spring. Also, the Arctic Ocean is not ice-filled in November and therefore the constraint and effect of coastal boundary conditions on ice deformation are less pronounced. Spatially, we see this in Figures 5 and 6. The higher fractional coverage of deformed cells in the seasonal ice zone is especially evident in November, December, and January. The differences between the two zones, based on deformation alone, are less distinctive after January. The upturn in deformation activity in April and May can perhaps be attributed to the changes in the atmospheric boundary layer associated with the upturn in insolation with the onset of spring.

[24] Another estimate of note is the coverage of undeformed ice in openings and ridged/rafted ice after closings; they are accounted for separately in the RGPS products. Figure 7c shows the change in deformed and undeformed ice coverage at the end of April. The RGPS estimates are of changes in coverage because their initial areas in November are not known. This average change in deformed ice coverage is ~15% in the SIZ and ~10% in the PIZ while the change in undeformed ice cover is ~20% in the SIZ and ~12% in the PIZ. Similarly, the changes in areal coverage of deformed cells in the five regions are shown in Figure 3b. These quantities are somewhat dependent on the ridging/rafting parameters discussed in the next section. Field data with estimates of these parameters are not generally available. However, these values can be compared to the data taken by the British Trans-Arctic Expedition in 1969 where *Koerner* [1973] reports that 17% of the surface in a transect between North Pole and Spitzbergen was covered by undeformed ice less than a year old (similar to the quantity estimated here).

4.3. Divergence and Vorticity in PIZ and SIZ

[25] At short timescales, sea ice moves on the average several degrees to the right of the geostrophic wind in the Arctic Ocean [*Thorndike and Colony*, 1982]. Larger turning angles during the summer are explained by the structure of the atmospheric boundary layer (stability effects) and in part by the reduction of internal ice stresses [*Thorndike and Colony*, 1982]. Because of this turning angle, it is sometimes thought that there would be a relationship between the divergence of the ice cover and that estimated from spatial variations of the wind field, i.e. divergence/convergence is associated with the large-scale cyclonic/anticyclonic motion of the ice cover. The notion is, if indeed a relation exists,

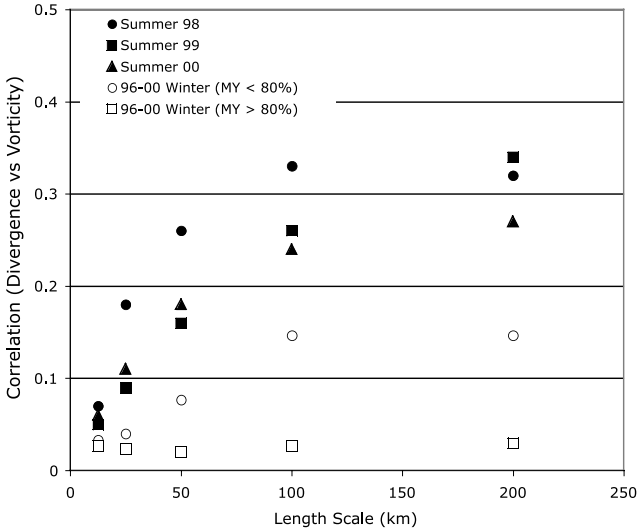

Figure 8. Seasonal and regional correlations between divergence and vorticity at different length scales. The significance of the reported correlations is all at the 0.01 level.

that changes in ice concentration could be related to the sense of rotation of the ice cover; this is examined here with RGPS observations.

[26] Using buoy motion, *Thorndike and Colony* [1982] find that only an insignificant fraction of the ice cover divergence is accounted for by predictions calculated from the observed atmospheric pressure fields. They suspect that the true ice divergence is obscured by measurements errors; the divergence is small because the ice velocity is turned only slightly from the direction of geostrophic wind. With small signal in the divergence and large noise in the estimated velocity and pressure derivatives, any true correlation may be completely masked. They also point out that internal ice stress may strongly affect divergence, thus reducing the correlation with the wind.

[27] From a restricted period during the summer (July–September) of 1980, *Serreze et al.* [1989] examined the same relationship with a denser buoy network and report that 40–70% of the divergence over the central Canada Basin can be explained by gradients of the local geostrophic wind. The implication is that if this relationship were robust that it would facilitate the prediction of new ice and brine production under these conditions.

[28] Here, we examine this relationship between divergence and vorticity of the ice cover at different length scales using the more extensive RGPS data set. Instead of comparing the observed divergence with that predicted from the wind field, we compute the direct correlation between the two RGPS quantities. At larger length scales, the vorticity of the ice cover should be an expression of the gradients associated with the large-scale advective component of the motion field. The relevant questions are: Are there significant correlations between local divergence and vorticity?; and, is the net divergence/convergence associated with the larger scale cyclonic/anticyclonic motion of the ice cover?

[29] The correlations between the two quantities under different conditions are plotted in Figure 8. We separate the winter (Oct–May) RGPS data set into regions in the perennial ice zone (MY > 80%) and seasonal ice zone (MY < 80%). For the summer (Jun–Aug), we could not separate the data into ice zones because the lack of backscatter contrast between MY and FY ice for ice type classification due to surface melt. The winter correlations in the PIZ are lumped together as the correlations are negligible for all four winters at length scales up to 200 km. It can be seen that the correlations are slightly higher in the SIZ and increase with length scale. During the summer, even though the correlations are higher at longer length scales, vorticity accounts for only ~10% of the observed divergence.

[30] First, the results (Figure 8) show that at short length scales the correlations are weak to negligible. Below 10–20 km, the deformation is potentially dominated by the gradients due to fractures (openings, closings, and shearing leads) in the ice cover that may or may not be correlated with the large-scale field. Also, the larger noise level near the scale of the RGPS cells (~10 km) compared to the averaged quantities at longer length scale may decorrelate the quantities in question. Above 20 km, the correlations increase with length scale. As mentioned above, the area-averaged vorticity is more representative of the gradient associated with the large-scale advective component of the motion field; and, it is this general relationship between divergence/convergence and cyclonic/anticyclonic motion at the large scale that is of interest.

[31] Second, at all length scales the correlations increase from ice conditions in the winter PIZ, to that in the winter SIZ, and to that of the summer ice cover. This is most likely attributed to ice strength and compactness: thicker ice in the winter PIZ, thinner ice in the winter SIZ, and the reduced compactness or lower ice concentration in the summer. The small interannual variability of the summer correlations at different length scales indicates that these relationships are indeed representative or typical for the years examined. This dependence would imply that as the ice cover gets thinner in a warming climate, the vorticity may account for a higher fraction of the divergence (even though still small) than is seen here.

[32] The correlations here are comparable to that reported by *Thorndike and Colony* [1982] but certainly lower than that reported by *Serreze et al.* [1989]. The differences between the data sets are as follows: (1) Even though the RGPS data set provides a much higher density of observations, the spatial gradients in ice motion are from 3-day displacements compared to the daily observations from buoy analyses; (2) The velocity gradients are computed at shorter length scales <200 km – buoy separations are typically greater 500 km; and, (3) the RGPS sampling is biased toward regions where the ice cover is more compact. We also note that the correlations are between two estimated quantities and errors in these quantities would lower the true correlations. *Lindsay and Stern* [2003] estimate the uncertainty in divergence computed at individual cells (~10 km on a side) to be ~0.035/day, *Kwok and Cunningham* [2002] give an uncertainty of 0.01–0.04/day by examining the RGPS data and through numerical simulation. The uncertainties in RGPS divergence and vorticity are substantially reduced at larger length scales (>10 km) when these quantities are spatially averaged. The uncertainty in diver-

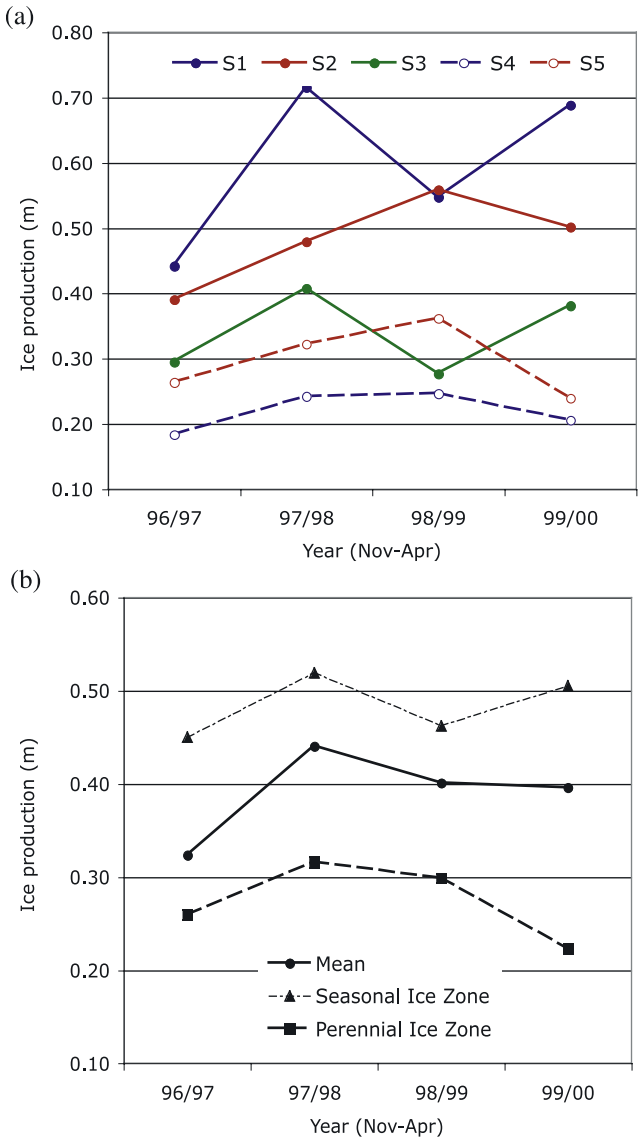

Figure 9. Deformation-related ice production (November through May). (a) Regional. (b) Perennial and seasonal ice zones.

gence computed from buoy displacements are higher and depends very much on the separation of the displacement estimates. At 100 km separation, using the analysis prescribed by *Thorndike and Colony* [1982], the uncertainty in divergence is ~0.04/day. This can be compared to an uncertainty of 0.004/day using 100 RGPS cells (the RGPS uncertainty divided by $1/\sqrt{N}$ where N = 100 cells). An additional issue with buoy estimates is the advection of unaccounted for material (sea ice) through the sides of polygons formed with buoy arrays.

5. Ice Volume Production

[33] The seasonal ice volume produced in openings or fractures in the ice cover is examined here. We first provide a brief review of the approach detailed in *Kwok et al.* [1995] and *Kwok and Cunningham* [2002]. Next, we discuss the regional ice production and contrast the differences in seasonal ice produced in the perennial and seasonal ice zones. Finally, remarks regarding the uncertainties of these estimates are provided.

5.1. Ice Production Estimates

[34] The thickness distributions in the RGPS products are of only seasonal ice created in openings of the ice cover since the initial observation. Basal ice growth of existing ice is not included; the thickness distribution within an RGPS cell, prior to the first observation, is not known. New ice is assumed to grow in openings; sea ice is ridged or rafted when the ice cover converges. Thus, only the ice volume and thickness due to seasonal ice growth are estimated. The seasonal ice thickness distribution, $g_s(h)$, is estimated from cell area changes using an ice growth model and an assumed mechanical redistribution function for sea ice. The ice growth rate is approximated as a function of the number of freezing-degree days experienced by each age category using Lebedev's parameterization [*Maykut*, 1986] where $h = 1.33\,F^{0.58}$. h is ice thickness (cm) and F is the accumulated freezing-degree days (K) derived from the IABP/POLES 2-m air temperature. The thickness redistributor uses a combination of rafting and pressure ridging to account for decreases in cell area. Ice less than 40 cm thick is rafted instead of ridged. Rafted ice is twice its original thickness and occupies half the area; ridged ice is five times its original thickness [*Parmerter and Coon*, 1972] and occupies a quarter of the area. At every time step, the thickness distribution within a cell is updated. In the RGPS products, the seasonal thickness distributions of undeformed ice in the openings and ridged/rafted ice are tracked separately.

5.2. Ice Production

[35] The seasonal ice volume produced in each subregion between the months of November and April are shown in Figure 9a. Differences can be related to the regional magnitude and temporal variability of deformation over the winter (Figure 7). Higher and more active deformation is associated with higher ice production. S_1 and S_2, in the southern Beaufort and Chukchi Seas, are active deformation zones that produce more ice than the other three. In addition to the net seasonal deformation, it should be emphasized that the shorter scale spatial and temporal variability in deformation is also conducive to ice production: simultaneous local openings and closings can sum up to negligible net divergence even though ice is produced in openings. In fact, even though S_2 decreased in area over three of the four years ice production is comparable to that of S_1.

[36] Ice production ranges from ~0.2 m in S_4 (central Arctic) to ~0.7 m in S_1 (Beaufort Sea). As a reference, 0.1 m of ice over the Arctic Ocean is equivalent to 4% of the Arctic ice volume (assuming an average thickness of ~2.5 m) or >30% of the average Fram Strait outflow [*Kwok et al.*, 2004]. The regional variability is high. Because the sea ice growth rate is non-linear and is much higher in new openings, this adds to the basal growth of the background ice cover at the beginning of the growth season. This statement assumes that deformed ice has negligible effect on the growth rate of background ice cover. At ~10–15% coverage (Figure 7c), this is not an unreasonable assumption.

[37] Figure 9b compares the four years of sea ice produced in the seasonal and perennial ice zones between

November and April. On average, ~0.38 m is produced with ~0.5 m from the SIZ and ~0.3 m from the PIZ. Again, the regional differences and the differences between the two zones can be attributed to thickness and therefore mechanical strength, and the constraint and effect of coastal boundary conditions on ice deformation during the early winter. The 97/98 season produced significantly more ice (>0.1 m) compared to the lowest winter of 96/97. Compared to the PIZ, the ice production in the SIZ is larger by a factor that ranges from 1.5 to 2.3 over the four years.

[38] The contribution of deformation-related ice growth to the total Arctic mass balance can be approximated. Available estimates of annual sea ice growth and melt in the central Arctic Ocean are summarized in Table 1 of *Steele and Flato* [2000]. The only mass balance observations from a transect of varying ice thickness [*Koerner*, 1973] in the PIZ give an annual growth of ~1.1 m. This annual mean approximately doubles that of the basal growth of ~0.5 m over 3 m ice [*Untersteiner*, 1961]. Model estimates of annual production ranges between 1.1–1.3 m. Our 6-month results in the PIZ and the regions in the central Arctic (Figure 9) show that deformation-related ice production contributes ~0.2–0.3 m. Scaling to an 8-month growth season, this is approximately 25–40% of the total ice production of ~1 m in the central Arctic. As a point of comparison, using data from the same transect, *Koerner* [1973] estimates that 20% of the total ice production in the Arctic Ocean is related to deformation.

[39] For the seasonal ice zone, we offer a rougher estimate of the contribution of deformation-related ice production. In the absence of deformation, as a rule of thumb undisturbed thermodynamic growth in the SIZ contributes between 1.5–2 m to the total ice production [*Steele and Flato*, 2000] and the interannual variability is probably high and dependent on a number of factors including timing of freeze up and the record of atmospheric/oceanic forcing of a particular winter. From the SHEBA field measurements in 1998, *Perovich et al.* [2003] report that the total accretion during the 9-month growth season is >1 m for young ice. Deformation contributes to this total by fractures in the ice cover renewing areas of open water where more rapid ice growth can occur in place of thicker ice. If the deformation-related ice production is ~0.5 m in the SIZ, it could add 25–40% (after scaling to 8 months) of net ice production to a background of basal growth. This value would be higher if the SHEBA values were indicative of current conditions. Thus, deformation-related ice production could account for a large fraction of the mass budget in the SIZ.

5.3. Uncertainties in Ice Production

[40] The uncertainties in ice production are discussed in *Kwok and Cunningham* [2002] which we will review briefly and add to some of that discussion. All the RGPS cells are surveyed nominally once every three days and the area changes are net changes over that interval. This temporal sampling strategy of the cell area means that opening and closing events over the interval resulting in zero net area change would be missed. An opening followed by closing within a three-day interval would introduce an ice volume stored in ridged/rafted ice that is unaccounted for in the RGPS record. Similarly, a closing followed by an opening result in unaccounted for volume in ridged/rafted ice and the introduction of an undeformed ice area. The consequence is then an underestimation of the sea ice volume produced over a 3-day period. Also associated with the 3-day sampling is the uncertainty in the exact time of occurrence of an opening or closing event. Using the ice growth model here, a sampling interval of three days would cause an average uncertainty in ice age of 1.5 days or an uncertainty in the thickness of the thinnest ice of about 12 cm assuming an air temperature of −30°C. As the ice gets thicker, the growth rate slows and the uncertainty in thickness decreases.

[41] In fact, *Kwok et al.* [2004] have shown that new ice production due to the recurrent openings and closings at subdaily timescales, even though small, if ubiquitous could contribute to ice production within the winter pack. They estimate that this process could account for an equivalent of 5 cm of ice thickness over 6 months of winter in the central Arctic, approximately ~10% of the basal ice growth of ~0.5 m. No estimates are available from the seasonal ice zone. This may however be a small contribution to the overall uncertainty.

[42] Straight-line segments connecting the cell vertices define the RGPS cell boundaries. The sides of these cells are not the actual boundaries of the material element. Floes smaller than the cell dimensions could advect in and out of these boundaries. Inspection of SAR imagery shows that this does not happen often since most deformations are along leads between rigid plates during the winter and independent motion of small floes are not observed.

[43] The ice motion field is not a continuous, differentiable field since the deformation is localized along linear features. At discontinuities, (e.g., slip lines, leads) sometimes unfavorable geometric location of the grid points relative to these linear features would lead to inadequate spatial sampling of the deformation and cause spurious openings and closings of the ice cover. The errors introduced in this case would be dependent on the direction of the discontinuity relative to the orientation of the sampling grid. This effect would result in an overestimation of the volume production.

[44] The factors above could potentially affect the overall estimates of deformation-related ice production. Validation of the RGPS thickness estimates is difficult because of the spatial scale involved and the lack of coincident field observations. In one study, *Yu and Lindsay* [2003] compared the thin ice thickness distributions derived from the advanced very high-resolution radiometer (AVHRR) with RGPS estimates over the Beaufort Sea and the Canada Basin for the period December 1996 to February 1997. The comparisons show a compelling agreement. High correlations were found in cases where thin ice grew in large, wide leads extending several hundred kilometers. At these large scales, estimates from AVHRR images and RGPS showed similar amounts of thin ice in leads. However, when major surface deformation occurred on small scales (100 m to 10 km), the finer spatial resolution (100 m) of RADARSAT images enabled the RGPS algorithm to derive more thin ice than that of AVHRR. Under such conditions the correlation between the two dropped, and a small negative bias (about 1%) was observed in the estimates from AVHRR. This bias, mostly concentrated at the very thin end of the thickness distribution, caused a deficit in the AVHRR-derived thin ice growth. Although the AVHRR and RGPS algorithms treat

snowfall differently in the ice thickness calculations, both snow assumptions appear reasonable. However, RGPS may underestimate the thin ice production because of the 3-day sampling interval.

6. Conclusions

[45] In this paper we examined the deformation and ice production regionally and in the perennial and seasonal ice zones using four years of data from the RGPS. We find that all regions exhibit a seasonal behavior in deformation activity with the most active months in November, December, and January. The ice cover remains relatively inactive between February and April but the activity increases in spring. Net deformation is largest in the regions with significant open water boundaries in the late fall and early winter. This distinction is seen more clearly in the differences in deformation activity in the seasonal and perennial ice zones. There is higher deformation, up to two times more deformed cells, in the seasonal ice zone and this ratio is more pronounced during the late fall and early winter. This seasonality can be attributed partly to increasing thickness and therefore mechanical strength; the absence of the constraints and the effects of coastal boundary conditions on ice deformation in the early growth season; and, the seasonal structure of the atmospheric boundary layer (reduced momentum transfer due to the stability effects in winter). The upturn in deformation activity in April and May is most likely due to the changes in the atmospheric boundary layer associated with increasing insolation with the onset of spring. We also show that the correlation between divergence and vorticity is insignificant at length scales up to 200 km even though it is slightly higher during the summer. This result indicates that the relationship between divergence and the cyclonicity of the large- scale circulation pattern is weak in the Arctic Ocean. As the ice cover gets thinner and less compact in a warming climate, vorticity may account for a higher fraction of the divergence in the summer.

[46] The relationship between deformation and ice production in the SIZ and PIZ is clearly demonstrated. Increased ice production can be seen in regions with higher deformation activity. Comparatively, ice production is higher in the seasonal ice zone than the perennial ice zone. Between November and April, on average, $\sim$0.38 m is produced with $\sim$0.5 m from the SIZ and $\sim$0.3 m from the PIZ. During an 8-month growth season, our results in the PIZ and the regions in the central Arctic (Figure 8) show that deformation-related ice production could contribute $\sim$25–40% to the total of $\sim$1 m of ice production. For the seasonal ice zone, deformation-related ice growth could also add up to 25–40% of net ice production to a background of basal growth. These results suggest that deformation-related ice production may be an important component in the total mass budget.

[47] The present findings may have important oceanographic and atmospheric implications. Current estimates show a $-$9%/decade trend in the perennial ice coverage [*Comiso*, 2002] compared to a $-$3%/decade rate in the decrease of the total ice extent in the Northern Hemisphere. Coverage of seasonal ice is now at $\sim$40% of the Arctic Ocean [*Kwok et al.*, 2003] with the largest expanse covering the southern Beaufort. If deformation-related ice production is higher in the SIZ, the positive trend in seasonal ice coverage enhances new ice production and regions of brine production off the shelf. Large sensible heat-flux through these areas represents a substantial source of atmospheric heat in winter. By itself, this deformation-ice production relationship may be considered a negative feedback where weaker/thinner seasonal ice allowing more deformation-related ice production would adjust more quickly to thermodynamic perturbations from an equilibrium state. Potentially, this could enhance the growth-thickness relationship discussed in *Bitz and Roe* [2004] where thinner ice, with higher growth rates, acts as a stronger negative feedback mechanism to sea ice thinning due to climate perturbations. Thinner ice, in contrast to thicker ice, need not thin much to increase its growth rate a great deal, thereby establishing a new equilibrium with relatively little change in thickness.

[48] While it is clear that deformation-related ice production contributes positively to the mass budget, its overall effect in the face of increasing seasonal and thinner/weaker sea ice coverage may be more complicated. By decreasing the stability of the water column and thus promoting overturning with warmer, deeper waters, the brine rejection might also act to keep the ice thin. Also, recent work by *McPhee et al.* [2005] suggest that confined zones of upwelling of the pycnocline associated with significant shear motion of sea ice may greatly enhance local ocean-to-ice heat transfer and thinning of the winter ice cover. Thus, the net effect of deformation may be positive or negative especially in the face of a thinning ice cover: the reduction in ice strength in both the SIZ and PIZ increases deformation and promotes winter ice production in new openings while the oceanographic response may act to reduce the impact on the ice mass balance. Present ice-ocean models do not have adequate representation of these small-scale processes to fully examine the significance of their atmospheric and oceanographic implications.

[49] Compared to the results here, we suspect that the deformation and ice production statistics will change with a thinning ice cover [*Rothrock et al.*, 2003] and reductions in perennial ice coverage. The four years of results shown here may not be representative of the variability of the full range of behavior of the sea ice cover. RADARSAT data of the Arctic Ocean is still being acquired and we expect another 4–5 years of RGPS data will be available for examining the longer term behavior of the small-scale kinematic and dynamic processes of the Arctic Ocean sea ice cover.

[50] **Acknowledgments.** I wish to thank G. F. Cunningham and S. S. Pang for their assistance during the preparation of this manuscript. The RADARSAT imagery are processed and calibrated at the Alaska Satellite Facility, Fairbanks, AK. The RGPS is a joint project of the Alaska Satellite Facility and the Jet Propulsion Laboratory. R. Kwok performed this work at the Jet Propulsion Laboratory, California Institute of Technology, under contract with the National Aeronautics and Space Administration.

References

Babko, O., D. A. Rothrock, and G. A. Maykut (2002), Role of rafting in the mechanical redistribution of sea ice thickness, *J. Geophys. Res.*, *107*(C8), 3113, doi:10.1029/1999JC000190.

Bitz, C. M., and G. H. Roe (2004), A mechanism for the high rate of sea ice thinning in the Arctic Ocean, *J. Clim.*, *17*, 3623–3632.

Comiso, J. C. (2002), A rapidly declining perennial sea ice cover in the Arctic, *Geophys. Res. Lett.*, *29*(20), 1956, doi:10.1029/2002GL015650.
Coon, M. D., G. S. Knoke, D. C. Echert, and R. S. Pritchard (1998), The architecture of an anisotropic elastic-plastic sea ice mechanics constitutive law, *J. Geophys. Res.*, *103*(C10), 21,915–21,925.
Cunningham, G. F., R. Kwok, and J. Banfield (1994), Ice lead orientation characteristics in the winter Beaufort Sea, paper presented at IGARSS, Pasadena, Calif.
Curry, J. A., J. L. Schramm, D. Perovich, and J. O. Pinto (2001), Applications of SHEBA/FIRE data to evaluation of snow/ice albedo parameterizations, *J. Geophys. Res.*, *106*, 15,345–15,355.
Fily, M., and D. A. Rothrock (1990), Opening and closing of sea ice leads: Digital measurements from synthetic aperture radar, *J. Geophys. Res.*, *95*(C1), 789–796.
Hibler, W. D., III, and E. M. Schulson (2000), On modeling the anisotropic failure of flawed sea ice, *J. Geophys. Res.*, *105*(C7), 17,105–17,120.
Hopkins, M. A., J. Tuhkuri, and M. Lensu (1999), Rafting and ridging of ice sheets, *J. Geophys. Res.*, *104*(C6), 13,605–13,613.
Kalnay, E., et al. (1996), The NCEP/NCAR 40-year reanalysis project, *Bull. Am. Meteorol. Soc.*, *77*, 437–471.
Koerner, R. M. (1973), The mass balance of the sea ice of the Arctic Ocean, *J. Glaciol.*, *12*, 173–185.
Kwok, R. (2000), Recent changes of the Arctic Ocean sea ice motion associated with the North Atlantic Oscillation, *Geophys. Res. Lett.*, *27*(6), 775–778.
Kwok, R. (2001), Deformation of the Arctic Ocean sea ice cover: November 1996 through April 1997, in *Scaling Laws in Ice Mechanics and Dynamics*, edited by J. Dempsey and H. H. Shen, pp. 315–323, Springer, New York.
Kwok, R. (2002), Arctic Ocean sea ice area and volume production: A contrast of two years – 1996/97 and 1997/98, *Ann. Glaciol.*, *34*, 447–453.
Kwok, R., and G. F. Cunningham (2002), Seasonal ice area and volume production of the Arctic Ocean: November 1996 through April 1997, *J. Geophys. Res.*, *107*(C10), 8038, doi:10.1029/2000JC000469.
Kwok, R., E. Rignot, B. Holt, and R. G. Onstott (1992), Identification of sea ice type in spaceborne SAR data, *J. Geophys. Res.*, *97*(C2), 2391–2402.
Kwok, R., D. A. Rothrock, H. L. Stern, and G. F. Cunningham (1995), Determination of ice age using Lagrangian observations of ice motion, *IEEE Trans. Geosci. Remote Sens.*, *33*(2), 392–400.
Kwok, R., G. F. Cunningham, and W. D. Hibler III (2003), Subdaily ice motion and deformation from RADARSAT observations, *Geophys. Res. Lett.*, *30*(23), 2218, doi:10.1029/2003GL018723.
Kwok, R., G. F. Cunningham, and S. S. Pang (2004), Fram Strait sea ice outflow, *J. Geophys. Res.*, *109*, C01009, doi:10.1029/2003JC001785.
Lindsay, R. W. (2002), Ice deformation near SHEBA, *J. Geophys. Res.*, *107*(C10), 8042, doi:10.1029/2000JC000445.
Lindsay, R. W., and H. L. Stern (2003), The RADARSAT geophysical processor system: Quality of sea ice trajectory and deformation estimates, *J. Atmos. Oceanic Technol.*, *20*, 1333–1347.
Maykut, G. A. (1986), The surface heat and mass balance, in *Geophysics of Sea Ice, Ser. B, Physics*, vol. 146, edited by N. Untersteiner, pp. 395–463, Springer, New York.
McPhee, M., R. Kwok, R. Robbins, and M. Coon (2005), Upwelling of Arctic pycnocline associated with shear motion of sea ice, *Geophys. Res. Lett.*, *32*, L10616, doi:10.1029/2004GL021819.
Overland, J. E., S. L. McNutt, and S. Salo (1998), Arctic sea ice as a granular plastic, *J. Geophys. Res.*, *103*(C10), 21,845–21,867.
Parmerter, R. R., and M. Coon (1972), Model of pressure ridge formation in sea ice, *J. Geophys. Res.*, *77*, 6565–6575.
Perovich, D. K., T. C. Grenfell, J. A. Richter-Menge, B. Light, W. B. Tucker III, and H. Eicken (2003), Thin and thinner: Sea ice mass balance measurements during SHEBA, *J. Geophys. Res.*, *108*(C3), 8050, doi:10.1029/2001JC001079.
Richter-Menge, J. A., et al. (2002), Relating arctic pack ice stress and deformation under winter conditions, *J. Geophys. Res.*, *107*(C10), 8040, doi:10.1029/2000JC000477.
Rothrock, D. A., J. Zhang, and Y. Yu (2003), The arctic ice thickness anomaly of the 1990s: A consistent view from observations and models, *J. Geophys. Res.*, *108*(C3), 3083, doi:10.1029/2001JC001208.
Serreze, M. C., R. G. Barry, and A. S. McLaren (1989), Seasonal variations in sea ice motion and effects on sea ice concentration in the Canada Basin, *J. Geophys. Res.*, *94*(C8), 10,955–10,970.
Steele, M., and G. Flato (2000), Sea ice growth, melt, and modeling, in *The Freshwater Budget of the Arctic Ocean*, edited by E. L. Lewis, pp. 549–587, Springer, New York.
Stern, H. L., and R. E. Moritz (2002), Sea ice kinematics and surface properties from RADARSAT synthetic aperture radar during the SHEBA drift, *J. Geophys. Res.*, *107*(C10), 8028, doi:10.1029/2000JC000472.
Stern, H. L., D. A. Rothrock, and R. Kwok (1995), Open water production in Arctic sea ice: Satellite measurements and model parameterizations, *J. Geophys. Res.*, *100*(C10), 20,601–20,612.
Thompson, D. W. J., and J. M. Wallace (1998), The Arctic Oscillation signature in the wintertime geopotential height and temperature fields, *Geophys. Res. Lett.*, *25*, 1297–1300.
Thorndike, A. S., and R. Colony (1982), Sea ice motion in response to geostrophic winds, *J. Geophys. Res.*, *87*(C8), 5845–5852.
Untersteiner, N. (1961), On the mass and heat budget of Arctic sea ice, *Arch. Meteorol. Geophys. Biokumatol., Ser. A.*, *12*, 151–182.
Yu, Y., and R. W. Lindsay (2003), Comparison of thin ice thickness distributions derived from RADARSAT Geophysical Processor System and advanced very high resolution radiometer data sets, *J. Geophys. Res.*, *108*(C12), 3387, doi:10.1029/2002JC001319.
Yu, Y., D. A. Rothrock, and J. Zhang (2001), Thin ice impacts on surface salt flux and ice strength: Inferences from advanced very high resolution radiometer, *J. Geophys. Res.*, *106*(C7), 13,975–13,988.

R. Kwok, Jet Propulsion Laboratory, California Institute of Technology, 4800 Oak Grove Dr., Pasadena, CA 91109, USA. (ron.kwok@jpl.nasa.gov)